Measurement of Neutrino Flux from Neutrino-Electron Elastic Scattering

J. Park,[1] L. Aliaga,[2,3] O. Altinok,[4] and D. Zhang[2]

(The MINERvA Collaboration)

[1] *University of Rochester, Rochester, New York 14610 USA*

[2] *Department of Physics, College of William & Mary, Williamsburg, Virginia 23187, USA*

[3] *Sección Física, Departamento de Ciencias, Pontificia Universidad Católica del Perú, Apartado 1761, Lima, Perú*

[4] *Physics Department, Tufts University, Medford, Massachusetts 02155, USA*

(Dated: October 27, 2015)

Abstract

Neutrino-electron elastic scattering is the only practically observable neutrino process which can be precisely predicted in the standard electroweak model without the use of neutrino-nucleus scattering information. As such, it may be used to directly measure the flux of neutrinos, which for accelerator-based beams is typically uncertain to $\sim 10\%$ due to uncertainties in hadron production and focusing. We have isolated a sample of 97 ± 12 neutrino-electron elastic scattering candidates in the segmented scintillator detector of MINERvA, after subtracting backgrounds and correcting for efficiency. We then show how this sample can be used to dramatically improve the uncertainty on the predicted NuMI flux. This constraint can be used by other NuMI-based experiments, and this technique is applicable to future multi-GeV energy neutrino beams.

PACS numbers: 13.15.+g,13.66-a

Neutrino-electron elastic scattering is precisely predicted in the electroweak standard model because it involves only the scattering of fundamental leptons. At tree level in the electroweak standard model and in the limit that $m_e \ll E_\nu \ll \frac{M_W^2}{2m_e}$,

$$\frac{d\sigma(\nu e^- \to \nu e^-)}{dy} = \frac{G_F^2 s}{\pi} \left[C_{LL}^2 + C_{LR}^2 (1-y)^2\right], \tag{1}$$

where G_F is the Fermi weak coupling constant, s is the Mandelstam invariant representing the square of the center-of-mass frame total energy, $y \equiv T_e/E_\nu$, and T_e is the electron kinetic energy. C_{LL} and C_{LR} are constants that depend on the neutrino flavor and whether the initiating particle is a neutrino or anti-neutrino. For muon and tau neutrinos, $C_{LL} = \frac{1}{2} - \sin^2\theta_W$ and $C_{LR} = \sin^2\theta_W$, where θ_W is the Weinberg angle, and for anti-neutrinos the values for C_{LL} and C_{LR} are swapped. For electron neutrinos (anti-neutrinos), the value of C_{LL} (C_{LR}) is instead $\frac{1}{2} + \sin^2\theta_W$ because the interaction contains interfering contributions from the neutral current interaction that is present for all flavors and a charged-current interaction present only for electron neutrinos. The kinematics of the reaction limit the magnitude of the 4-momentum transferred from the neutrino, q, to $-q\dot{q} \equiv Q^2 < s$. The final state electron angle with respect to the neutrino, θ, may be uniquely determined from the initial neutrino and final lepton energies by

$$1 - cos\theta = \frac{m_e(1-y)}{E_e}; \tag{2}$$

therefore at accelerator neutrino energies, where $m_e \ll E_\nu$, the final state electron is very forward. Electroweak radiative corrections for this cross section have been calculated at one-loop order [1] and are few percent corrections to the tree level expressions for GeV energy neutrinos. We include in our calculation of the radiative corrections additional low energy terms [2] and one-loop electroweak couplings from recent global fits to electroweak data [3].

Experimental measurements of $\nu_\mu e^-$ and $\bar{\nu}_\mu e^-$ elastic scattering have been performed by the CHARM [4], BNL-E734 [5] and, most precisely, by the CHARM-II [6] experiment. In addition, $\nu_e e^-$ scattering has been studied by the E-225 [7] and LSND [8] experiments at LAMPF, and $\bar{\nu}_e e^-$ scattering by the TEXONO [9] experiment. These measurements are limited in precision either by statistics of the neutrino-electron elastic scattering sample, knowledge of the incoming neutrino flux, or both. The uncertainty of the neutrino-electron scattering within the electroweak standard model is much smaller than the uncertainties associated with any of these measurements or their combination [3].

This unusual situation in neutrino scattering, in which the scattering cross section is much better known than it can be measured, offers the possibility of using the reaction as a standard candle from which one can derive contraints on the neutrino flux. The technical challenge that balances this promise is that the cross-section is small, roughly 10^{-4} of the total charged-current ν_μ cross-section, so the signal statistics are low and the backgrounds are substantial.

Given Eqn. 2 the signature for neutrino-electron scattering is a single electron with energy and angle satisfying $E_e\theta^2 < 2m_e$ and no other activity in the event. The dominant backgrounds come from electrons produced in charged current ν_e and $\bar{\nu}_e$ interactions, and decay photons from π^0 production. Therefore, the analysis selects low angle electrons, distinguighes them from photons, and rejects events with any other particles visible in the detector.

The MINERvA experiment uses the NuMI beam [10], which starts with 120 GeV protons which strike a graphite target. The mesons produced in $p + C$ interactions are focused by two magnetic horns into a 675 m long helium-filled decay pipe. The horns were set to focus positive mesons, resulting in a ν_μ-enriched beam. Muons produced in meson decays are absorbed in 240 m of rock downstream of the decay pipe. This analysis uses data taken between November 2010 and April 2014 with 3.5×10^{20} protons on target. The predicted flux of neutrinos for this exposure is shown in Figure 1.

The neutrino beam is simulated by a Geant4-based model [11, 12] which is constrained to reproduce hadron production measurements by NA49 on carbon [13]. FLUKA is used to translate NA49 measurements to proton energies between 12 and 120 GeV [14, 15]. The π/K ratio measured by MIPP on a replica NuMI target [16] is used to constrain production of kaons. Hadronic interactions not constrained by the NA49 or MIPP data are predicted using the FTFP hadron shower model[1].

The MINERvA detector consists of a core of scintillator strips surrounded by electromagnetic and hadronic calorimeters on the sides and downstream end of the detector[2] [17]. The strips are perpendicular to the z-axis (which is very nearly the beam axis) and are arranged in planes with a 1.7 cm strip-to-strip pitch[3]. Three plane orientations ($0°, \pm 60°$ rotations around the z-axis) enable reconstruction of the neutrino interaction point and tracks of outgoing charged particles. Forward electrons typically look like a single particle track near the neutrino interaction point at which they are created, and slowly develop in an electromag-

[1] FTFP shower model in Geant4 version 92 patch 03.
[2] The MINERvA scintillator tracking region is 95% CH and 5% other materials by weight.
[3] The y-axis points along the zenith and the beam is directed downward by 58 mrad in the y-z plane.

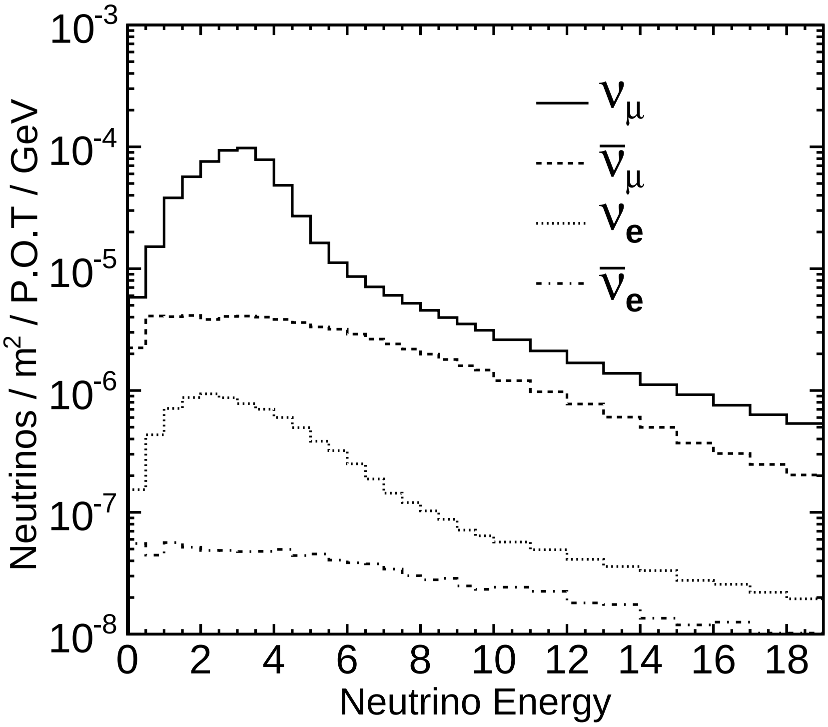

FIG. 1: The predicted flux of ν_μ, $\bar{\nu}_\mu$, ν_e and $\bar{\nu}_e$ for the dataset used in this analysis

netic cascade in the scintillator, which typically ends in the downstream electromagnetic calorimeter. The 3.0 ns timing resolution allows separation of particles from multiple interactions within a single beam spill. MINERvA is located 2 m upstream of the MINOS near detector, a magnetized iron spectrometer [18] which is not used directly in this analysis, but is used to reconstruct momentum of through-going muons for many calibrations [17] and to perform muon reconstruction efficiency studies described later.

The MINERvA detector's response is simulated by a tuned Geant4-based [11, 12] program. The energy scale of the detector is set by ensuring that both the photostatistics and the reconstructed energy deposited by momentum-analyzed through-going muons agree in data and simulation. The calorimetric constrants used to reconstruct the energy of electromagnetic showers and the correction for passive material are determined from the simulation. The applicability of this energy scale to electrons in the scintillator tracker is verified using a sample of Michel electrons from $\mu^\pm \to e^\pm \nu \bar{\nu}$ decays of muons stopping in the detector [17] and by the reconstructed invariant mass of identified $\pi^0 \to \gamma\gamma$ decays [19]. The uncertainty in the response of the detector to protons and charged pions is constrained by the measurements made with a scaled down version of the MINERvA detector in a low energy hadron test beam [20].

Neutrino interactions are simulated using the GENIE 2.6.2 neutrino event generator [21]. The neutrino-electron scattering cross section is described in the Introduction. For quasi-elastic interactions, the cross-section is given by the Llewellyn Smith formalism [22]. Vector form factors come from fits to electron scattering data [23]; the axial form factor used is a dipole with an axial mass (M_A) of 0.99 GeV/c^2, consistent with deuterium measurements [24, 25], and sub-leading form factors are assumed from PCAC or exact G-parity symmetry [26]. The nuclear model is the relativistic Fermi gas with a Fermi momentum of 221 MeV/c and an extension to higher nucleon momenta to account for short-range correlations [27, 28]. Inelastic, low W reactions are based on a tuned model of discrete baryon resonance production [29], and the transition to deep inelastic scattering is simulated using the Bodek-Yang model [30]. Final state interactions are modeled using the INTRANUKE package [21]. Coherent pion production is simulated using the model of Rein and Sehgal [31]. Uncertainties in the parameters of these models are assigned based on either measurement uncertainties from data or are assigned to cover differences between datasets and this model.

The MINERvA detector records the energy and time of energy depositions (hits) in each scintillator strip. Hits are first grouped in time and then clusters of energy are formed by spatially grouping the hits in each scintillator plane. Clusters with energy > 1 MeV are then matched among the three views to create a track. An energetic electron traverses about a radiation length as a minimum ionizing particle (MIP) until it begins to shower. The radiation length, X_0, corresponds to 25 scintillator planes when the direction of the electron is normal to the planes. The track-like part of an electron shower can be identified, and the beginning of that track serves as the event vertex. Occasionally, an electron starts to shower early and the MIP track is too short to be reconstructed as a track. In that case the isolated energy deposition is used to define the vertex location and shower direction which are inputs to the cone algorithm described below. The event vertex is restricted to be within the central 110 planes of the scintillator tracking region and no closer than 22 cm to any edge of the planes. These requirements define a region with a mass of 5.57 metric tons.

Once a track or an isolated energy deposition is identified, then a cone is identified using the vertex and angle of the identified object. The cone is defined to have an opening angle of 10 degrees with respect to the angle of the found track or energy deposit, and starts far enough upstream such that the width of the cone 80mm upstream of the vertex is 50mm wide. The cone extends far enough to capture the downstream remnants of the electromagnetic showers which sometimes fluctuate to only a single photon which later converts. The energy in the cone is calculated calorimetrically as defined above and is identified as the electron candidate energy. The resulting electron fractional energy resolution using this procedure is $5.9\%/\sqrt{E_e(GeV)} \oplus 3.4\%$ [32].

The accurate direction reconstruction of the electron shower is critical to background rejection of background using an $E_e\theta^2$ cut. The energies and locations of clusters inside the cone are fed into a Kalman filter to determine the electron angle with respect to the beam direction. Because the downstream end of an electron shower does not necessarily align with the original electron direction, only the first 30 energy depositions are used in the fit. The resulting average electron angular resolution is 0.41 (0.43) degrees in the horizontal (vertical) direction [32].

The times of the tracked hits are used to determine the interaction time. Other untracked clusters up to 20 ns before and 35 ns after that time are associated with the event. Energy within this reconstruction time window, but outside the electron cone, is used to search fro the presence of other particles in the event which would indicate that the event is a background rather than neutrino-electron elastic scattering event.

The majority of neutrino interactions in MINERvA come from charged current (CC) ν_μ interactions on nuclei either in or upstream of the detector. These events are easily removed by a cut requiring the energy in a 30 cm-diameter cylinder along the cone axis and upstream of the event vertex to be less than 300 MeV. Events are also removed if the end of the shower penetrates through more than 2 planes of the hadron calorimeter, corresponding to 5 cm of steel.

After the ν_μ CC interactions on nuclei are removed, the remaining background is from neutral current (NC) pion production or electron neutrino interactions on nuclei in the detector. These topologies can be removed by making cuts that ensure that the electron energy deposition is consistent with coming from a single particle that does not have hadronic interactions.

A minimum energy cut of 0.8 GeV is made to remove the significant background that arises from π^0 decays to photons, and to ensure good angular and energy reconstruction of the electron. In addition, the electron track is not allowed to bend by more than 9 degrees,

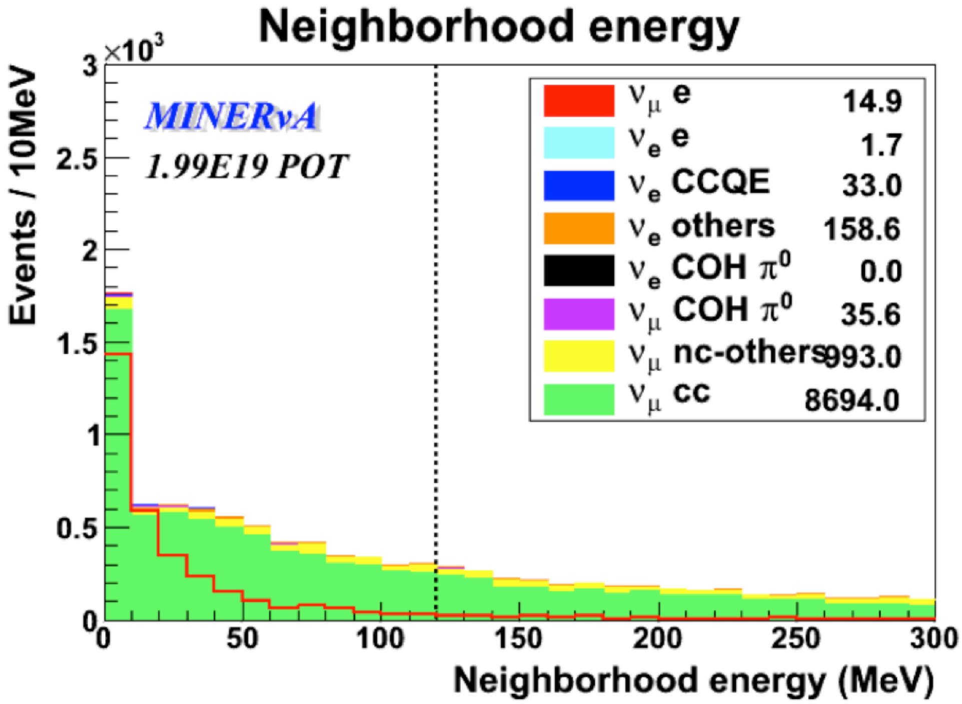

FIG. 2: PLOT IS ONLY A PLACEHOLDER: This plot shows the energy in a 5cm neighborhood of the electron cone after all cuts except a cut on this variable, for both the data, and the predicted signal and backgrounds after backgrounds have been tuned.

since this would be indicative of a hadronic scatter.

To ensure that there is only one particle that makes the energy present in the cone cuts are made on the transverse energy distribution, the longitudinal energy distribution, and finally the consistency of the energy depositions between the three views of the sinctillator planes.

There are two transverse energy deposition cuts made. First, the energy within 5 cm of the outer boundary of the electron cone is required to be less than 120 $(65 + 7.8 \times E_e)$ MeV for electrons that are less (greater) than 7 GeV in energy. This energy in the neighborhood of the electron cone is shown in Fig. 2. Second, for each view the energy-weighted RMS of the distance of each cluster of energy from the cone center must be less than 65 mm.

There are also two cuts made on the longitudinal energy distribution. The Kalman fitter that determines the electron angle returns a χ^2 describing the quality of the fit to a single particle energy deposition. A very loose cut of $\chi^2/NDF < 100$ is made to remove multiple particle showers without compromising the single-particle acceptance. In addition, the maximum energy deposition for one plane in the cone divided by the product of the distance between the start of the shower and that maximum energy and the shower energy is required to be less than 5, which is consistent with electromagnetic shower propagation in scintillator.

Finally, the energy deposition in the cone for each view relative to the other two views is required to be consistent with that of a single particle. When there are two ore more particles originating from the same vertex, they may overlap in one view of the cone but not in the other two views. Because there are twice as many planes in the X direction as in the U or V directions, the following two cuts remove events where two or more particles overlap inside the cone in one view not not all views:

$$\begin{aligned} |E_{XUV}| &= |\frac{E_X - E_U - E_V}{E_X + E_U + E_V}| < 0.28 \\ |E_{UV}| &= |\frac{E_U - E_V}{E_U + E_V}| < 0.5 \end{aligned}$$

where E_J is the energy deposited in the J view of the detector.

After the cuts above are made then the remaining backgrounds are primarily from electron neutrino quasi-elastic interactions, and events with single photons in them. The photons can be rejected by looking at the energy deposition per unit distance (dE/dx) at the beginning of the electron candidate track. For photons that convert, dE/dx is consistent with two electrons while the signal is made of only one electron. This cut is best made before the electron starts showering, but far enough into the track so that the photostatistics are adequate. The optimal distance for this analysis is to cut on the average energy deposition in the first four scintillator planes in the track. This average energy deposition, normalized by the cosine of the incident electron, is shown for data, and predicted signal and background events in Fig. 3. Events are required to have an average dE/dx less than $4.5MeV/1.7cm$.

After the dE/dx cut is made the remaining major background is from ν_e charged current quasi-elastic interactions (CCQE), namely $\nu_e n \rightarrow e^- p$ or $\bar{\nu}_e n \rightarrow e^+ n$. If the recoiling nucleon is not observed in the detector, which is common at low momentum transfer, the final state is a single electron or positron and cannot be distinguished from the signal using particle identication cuts. Given the kinematics described by Equation 2, and the small angle approximation, $E_e\theta^2$ must be less than the electron mass for neutrino electron scattering, but is much larger for neutrino nucleon scattering. Figure 4 shows the distribution of this

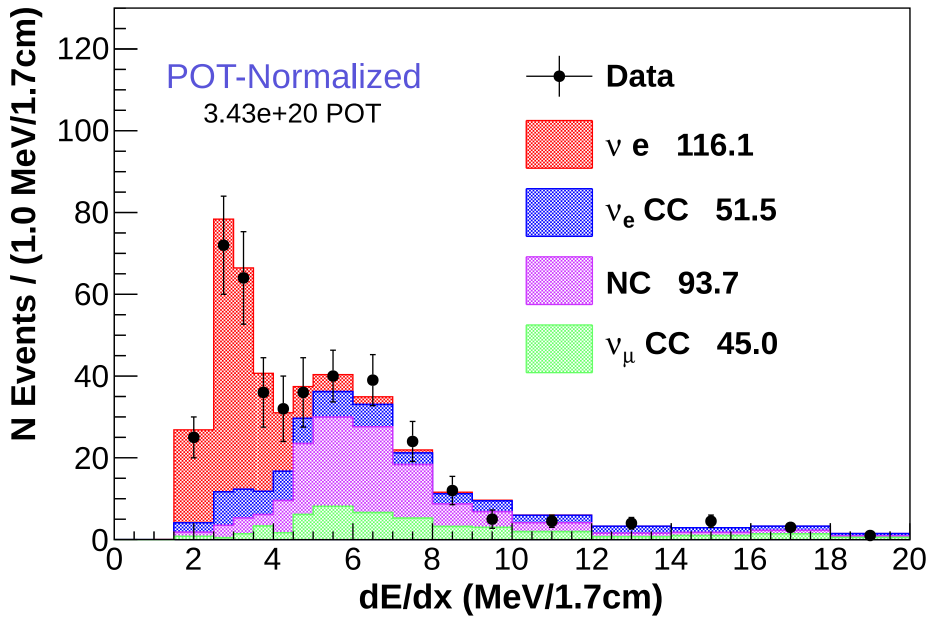

FIG. 3: The distribution of dE/dx after the cuts that isolate single electromagnetic showers are made, but before the final cuts are made.

variable for the data, and the signal and background predictions, after all cuts except this last one. Events with $E_e\theta^2$ greater than 0.0032 GeV Radian^2 are removed.

The $E_e\theta^2$ cut removes the ν_e CCQE background effectively at low energy, but is less effective for high energy electrons because those electrons are also produced at smaller angles, similar to neutrino electron scattering. As a secondary cut, the momentum trasnfer squared, Q^2, is reconstructed directly under the assumption of ν_e CCQE kinematics,

$$E_\nu = \frac{m_n E_e - m_e^2/2}{m_n - E_e + P_e \cos\theta}, \tag{3}$$

$$Q^2 = 2m_n(E_\nu - E_e) \tag{4}$$

where m_n is the neutron mass and other symbols are defined above. Events with $Q^2 <$ 0.02 GeV^2 are removed to reject high energy electron ν_e CCQE events.

As shown in Fig. 4, the number of predicted background events after the final event selection is a small fraction of the signal events. If the predicted background is subtracted from data distribution, then a measure of the number of neutrino-electron scattering events is obtained. This procedure is subject to systematic uncertainties in the prediction of the background because mis-modeling of the background and flux uncertainties both bias the

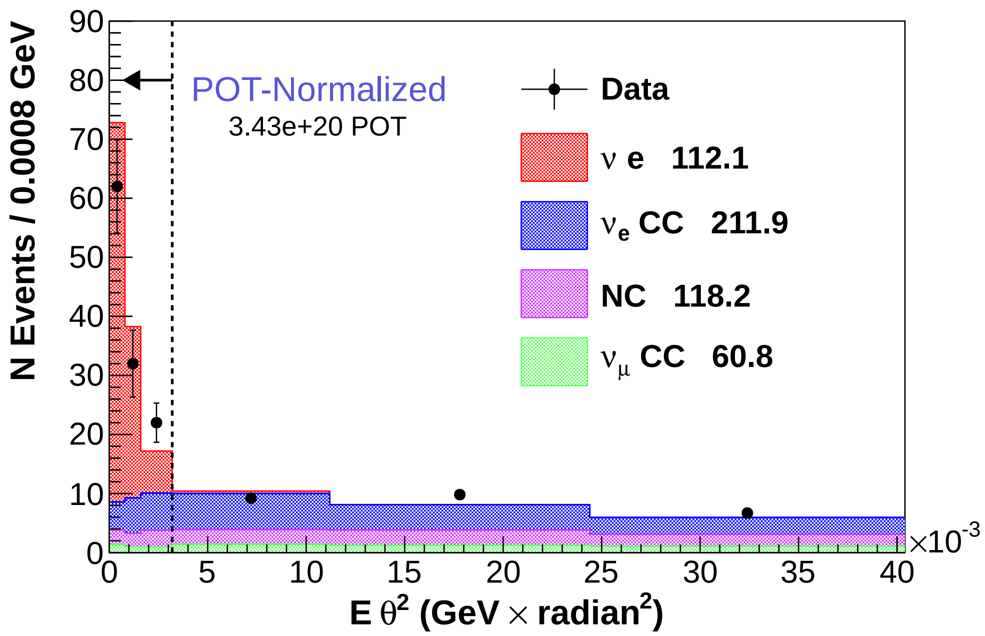

FIG. 4: The distribution of $E_e\theta^2$ after both the dE/dx cut and the cuts that isolate single electromagnetic showers are made.

signal measurement.

To reduce the background prediction uncertainty and the dependence of the backgrounds on an *a priori* flux prediction, the analysis normalizes the background prediction using events that fail the $E_e\theta^2$ cut but still pass a looser dE/dx cut. In addition, some of the cuts on the shower end transverse position and track length in the hadronic calorimeter were removed to allow more events into the sample. The sideband is defined to be all events with $E_e\theta^2 > 0.005\ GeV radian^2$ and $dE/dx < 20MeV/1.7cm$. This region is chosen with a high enough $E_e\theta^2$ value so that it does not contain any signal events, and with a low enough dE/dx value to only contain the populations of events that do leak into the final signal region.

However, this sideband still contains several different background sources which are themselves poorly constrained and have different extrapolations into the signal region. Therefore, this sideband is then divided into three distinct regions in order to determine overall normalizations for three different background sources: the sources from electron neutrinos, the sources from ν_μ charged current (CC) interactions, and the sources from ν_μ neutral current interactions, including coherent π^0 production. The three regions are defined as follows: the first region contains events with dE/dx above $3MeV/1.7cm$. The second two regions have dE/dx below $3MeV/1.7cm$ but are differentiated by having an electron energy above or below 1.2 GeV. The distributions of both the shower end transverse position and the fiducial track length in the hadron calorimeter are used in each of the three different regions, so the cuts on those variables are removed so that the information in the full range can be used for the fit. This is particularly helpful for constraining the ν_μ CC background. In the third region (which is ν_e enhanced), the maximum transverse RMS among the three views is also included in the fit.

The power of this procedure comes from the fact that the three different backgrounds have substantially different fractions in each of the three regions. The first region has roughly half its events from ν_μ CC events, one sixth from ν_e, and the rest are NC events. The second region is almost three quarters ν_μ CC events, one quarter ν_μ NC, with only a few per cent ν_e and NC coherent π^0 production. The third region is roughly half ν_e events, one quarter ν_μ CC events, with the remainder ν_μ NC and a few per cent NC coherent π^0. One background source, NC coherent π^0 production, is predicted from the simulation because that source cannot be enhanced in any sideband region.

A χ^2 is formed over all of the distributions defined above in each of the regions, and that χ^2 is minimized allowing three overall normalizations to float. The fit returns normalization constants of 0.76 ± 0.03 for the ν_e backgrounds, and 0.64 ± 0.03 (1.00 ± 0.02) for the ν_μ neutral (charged) current bbackgrounds. After the fit there is good agreement between the data and simulation for all the different distributions in the fit. In addition, both the dE/dx and $E_e\theta^2$ distributions are well-reproduced in the sideband regions after fitting.

The systematic uncertainties are classified as either the uncertainty in the background prediction or the uncertainty in the detector efficiency and acceptance. The systematic uncertainty, shown in Fig. 5, is evaluated by randomly changing the underlying simulation prediction according to the various uncertainties, refitting the background scale factors, and then subtracting the background, re-extracting the electron energy spectrum, and recorrecting for detector acceptance.

The largest uncertainties in the background prediction come from the flux and the background cross section models, although they are signficantly reduced by the sideband tuning procedure described above. The uncertainty in the electron energy scale (4%) is determined by comparing the agreement between data and simulation for the Michel electron

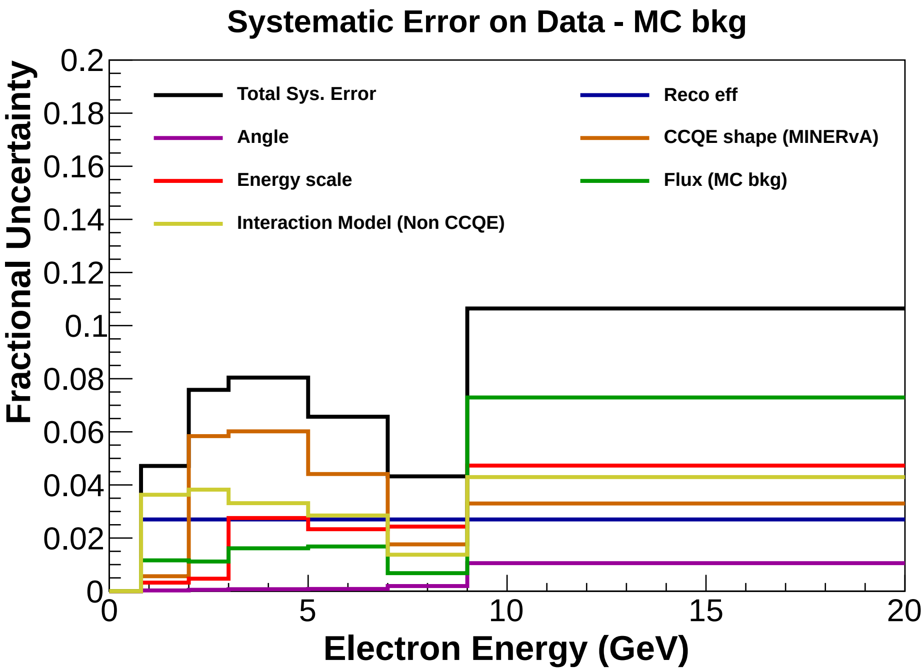

FIG. 5: The fractional systematic uncertainties as a function of the electron energy after all the cuts described above are made, and after the tuned background has been subtracted.

candidates. The uncertainty in the neutrino beam angle direction with respect to the detector axis (1 mrad) is determined by comparing the data and simulation for high energy ν_μ charged current events that have very low hadronic energy. Based on that study a correction of 3(1) mrad is made on the angle in the vertical (horizontal) direction. The flux uncertainties are incorporated by varying the parameters associated with hadron production and beam focusing in the flux model. The non-CCQE interaction model uncertainties are incorporated by varying the underlying parameters in the cross section models for processes such as resonance production and coherent scattering. The reconstruction efficiency uncertainty is determined by assuming that the reconstruction efficiency uncertainty for electrons is the same as it is for muons, since both particles' tracks are seeded using the same technique. The reconstruction efficiency uncertainty for muons is determined by comparing the data and simulation for the efficiency of matching a muon track in MINERvA once a track is found in MINOS that extrapolates into MINERvA. The discrepancy between data and simulation is treated as the systematic uncertainty.

The most important systematic uncertainty for electron energies below 7 GeV comes from the fact that the ν_e CCQE cross section shape as a function of Q^2 is not known precisely,

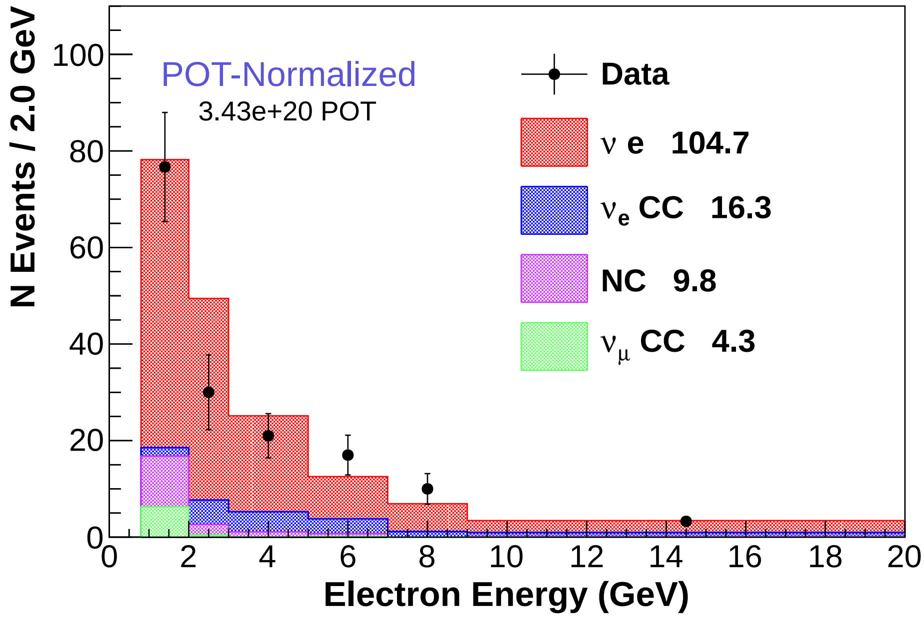

FIG. 6: The electron energy distribution for the data (black points) and predicted signal and backgrounds (stacked histograms) after all the cuts described in the text are made, and after the background tuning procedure is complete.

and for those electron energies the background at low Q^2 must be extrapolated using events at high $E_e\theta^2$, which are also at high Q^2. MINERvA measured a different cross section shape versus Q^2 than what is in the standard GENIE neutrino event generator [33], and the systematic is evaluated by taking the difference between the shape of the cross section as a function of Q^2 that MINERvA measured and the one predicted by GENIE. At higher electron energies, because of the minimum Q^2 cut, this uncertainty no longer dominates and the flux and the electron energy scale become the largest unertainties.

After all the cuts are made, there are a total of 127 candidates, with a prediction of $30.4 \pm 2.3(stat) \pm 3.3(syst)$ background events. The resulting electron energy spectrum is shown in Fig. 6. The simulation indicates that the product of acceptance and efficiency averaged across electorn energy is $73.3 \pm 0.5\%$ and varies between approximately 70% at the lower and upper ends of the spectrum and 78% at moderate electron energies. The electron energy spectrum after correcting for acceptance and efficiency is shown in Fig 7. The total number of background-subtracted, efficiency corrected events is 97 ± 12.

Although some of the intitial state neutrino's energy is lost to the final state neutrino in

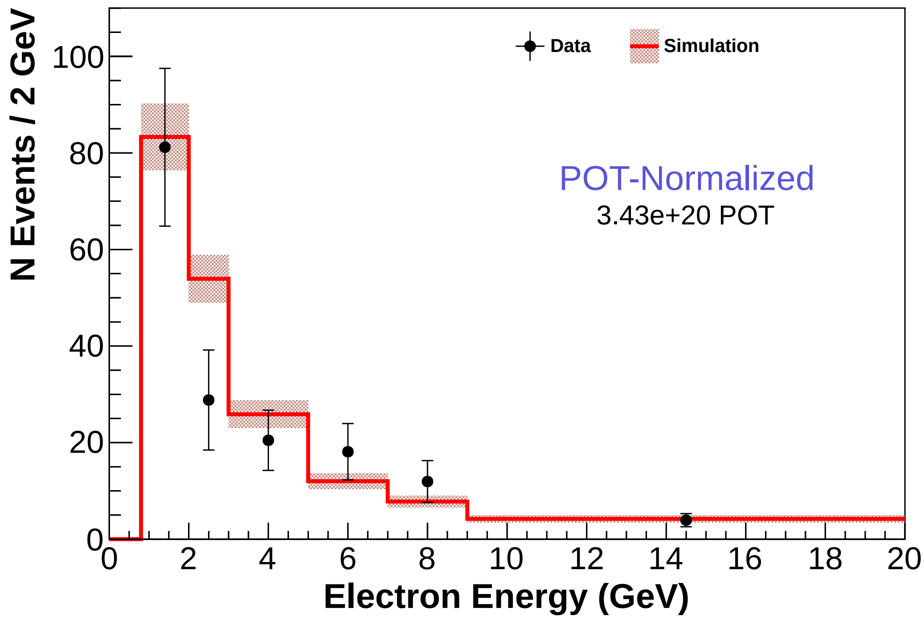

FIG. 7: The electron energy distribution for the data (black) and simulation (red) after all backgrounds are subtracted and after efficiency correction.

neutrino-electron scattering, the final state electron's energy spectrum can constrain both the overall normalization and shape of the neutrino flux. This can be done obvserving that Bayes theorem relates the probability of a particular flux model (M) given an observed electron spectrum $(N_{\nu e \to \nu e})$ to the *a priori* model and the probability of the data given the model:

$$P(M|N_{\nu e \to \nu e}) \propto P(M)P(N_{\nu e \to \nu e}|M), \tag{5}$$

and that, assuming a gaussian approximation of the poisson-distributed ddata, the probability of the data spectrum given the model is proportional to:

$$P(N_{\nu e \to \nu e})|M) \propto e^{-\chi^2_M} \tag{6}$$

where χ^2_M is the chi-square statistic comparing the observed electron energy distribution to that predicted by model M.

Fig. 8 shows the *apriori* probability distribution of the total number of neutrino-electron scattering events predicted in the simulation, obtained by randomly varying parameters of the simulation within their uncertainties 1000 times to create 1000 models or "universes". The uncertainty on the prediction is set by the precision in the hadron production measure-

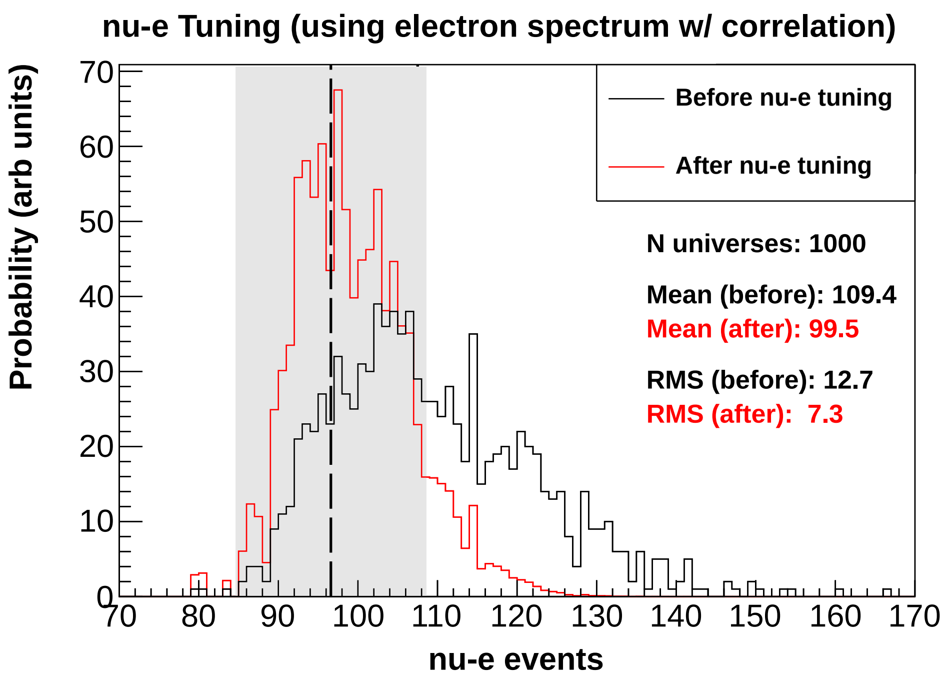

FIG. 8: The probability distribution (black) of the predicted number of neutrino-electron scattering events in the simulation given errors in the neutrino flux model and the modified probability distribution (red) given the observed electron energy spectrum.

ments, uncertainties in the beamline focusing system and alignment [34], and comparisons between different hadron production models in regions not covered by the NA49 or MIPP data.

For the case of electron-neutrino scattering, the only appreciably uncertain parameters in the simulation are those associated to the neutrino flux model. Also shown in Fig. 8 is the probability distribution given the observed neutrino-electron scattering spectrum, which is constructed by weighing the entry corresponding to a given universe by $e^{\chi_i^2}$, where the exponent evaluates the difference between the predicted neutrino-electron scattering energy spectrum in universe i and that observed in the data. The mean of the second, "constrained", distribtion is shifted down by 9% with respect to the original distribution, and the rms is reduced by approximately 40%. The same weights applied to produce this distribution can be used to constrain any other distribution predicted by the simulation. For example, the probability distribution of ν_μ flux integrated between 2 and 20 GeV before and after the constraint is shown in Fig. 9. The mean of this distribution is lowered by 8%, with ν_μ flux uncertainties as a function of neutrino energy modified as shown in Fig. 10. This method has

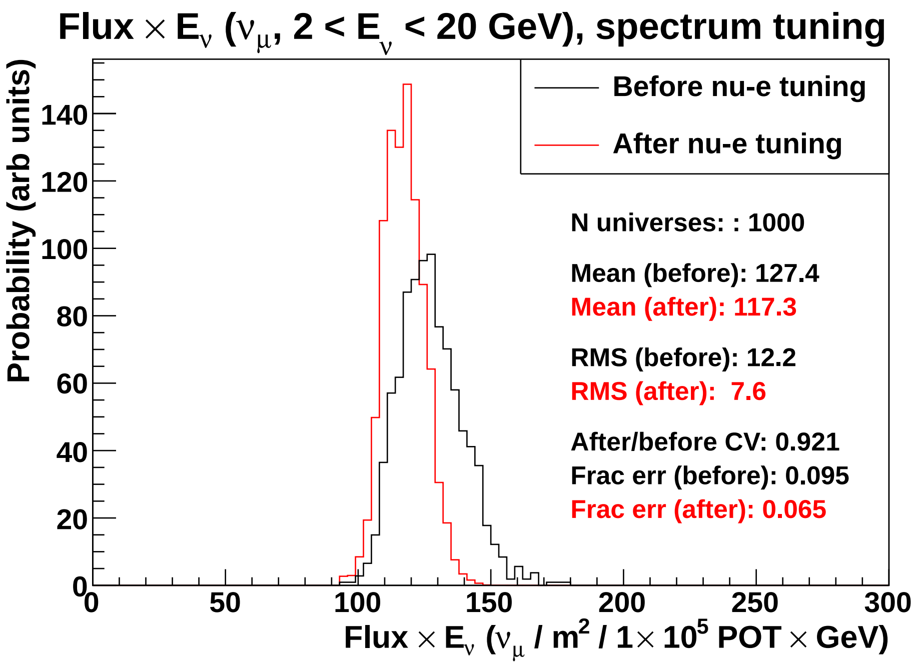

FIG. 9: The probability distribution (black) of the predicted ν_μ flux integrated between 2 and 20 GeV given errors in the neutrino flux model and the modified probability distribution (red) given the observed electron energy spectrum.

been applied to other MINERvA analyses [35], signficantly reducing the flux uncertainties on those measurements.

This measurement can also be used by other experiments operating in the NuMI beam who use a similar multi-universe method of propagating neutrino flux uncertainties and who are able to produce a predicted number of neutrino-electron scattering events with an electron enegy above 0.6 GeV in the fiducial mass and location given each of their simulated universes. That fiducial mass is centered at a point which is 1031.7 m from the upstream edge of the fist focusing horn in the NuMI beamline, and is located 0.264 m (0.129 m) from the NuMI beam horizontal (vertical) axis. The fiducial mass, defined as 5.77 metric tons, corresponds to $1.98 \pm 0.03 \times 10^{30}$ electrons, spread through a volume which is 2.48 m long and a hexagon of apothem 88.125 cm, tilted downward with respect to the beam axis by 58 mrad. Since the neutrino flux changes very little across this volume, the NuMI beam flux estimated at the center of this fiducial mass is a good approximation of the flux averaged over this volume (should we quantify this?).

This measurement is also an important proof of principle for a technique that could be

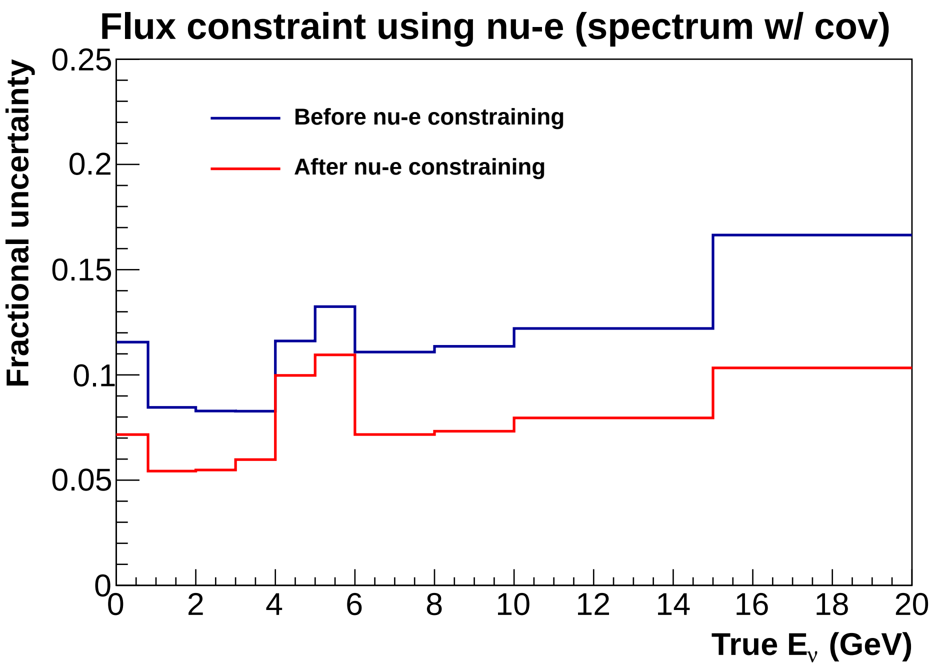

FIG. 10: The uncertainty on the predicted ν_μ flux before and after applying the $\nu e \to \nu e$ scattering constraint.

used for a future long baseline experiment, for example DUNE [36]. This measurement, because it involves scattering off electrons rather than nuclei, allows for any near detector technology with sufficient angular resolution and energy reconstruction to make a precise absolute flux prediction that for a few tons can achieve a measurement at the few per cent statistical preciison, given the expected neutrino fluxes.

This work was supported by the Fermi National Accelerator Laboratory under US Department of Energy contract No. DE-AC02-07CH11359 which included the MINERvA construction project. Construction support also was granted by the United States National Science Foundation under Award PHY-0619727 and by the University of Rochester. Support for participating scientists was provided by NSF and DOE (USA) by CAPES and CNPq (Brazil), by CoNaCyT (Mexico), by CONICYT (Chile), by CONCYTEC, DGI-PUCP and IDI/IGI-UNI (Peru), by Latin American Center for Physics (CLAF) and by RAS and the Russian Ministry of Education and Science (Russia). We thank the MINOS Collaboration for use of its near detector data. Finally, we thank the staff of Fermilab for support of the beamline and the detector.

[1] S. Sarantakos, A. Sirlin, and W. Marciano, Nucl.Phys. **B217**, 84 (1983).

[2] J. N. Bahcall, M. Kamionkowski, and A. Sirlin, Phys.Rev. **D51**, 6146 (1995), http://arxiv.org/abs/astro-ph/9502003 arXiv:astro-ph/9502003 [astro-ph] .

[3] J. Erler and S. Su, Prog.Part.Nucl.Phys. **71**, 119 (2013), http://arxiv.org/abs/1303.5522 arXiv:1303.5522 [hep-ph] .

[4] J. Dorenbosch *et al.* (CHARM), http://dx.doi.org/10.1007/BF01564701 Z.Phys. **C41**, 567 (1989).

[5] L. Ahrens, S. Aronson, P. Connolly, B. Gibbard, M. Murtagh, *et al.*, http://dx.doi.org/10.1103/PhysRevD.41.3297 Phys.Rev. **D41**, 3297 (1990).

[6] P. Vilain *et al.* (CHARM-II), http://dx.doi.org/10.1016/0370-2693(94)91421-4 Phys.Lett. **B335**, 246 (1994).

[7] R. Allen, H. Chen, P. Doe, R. Hausammann, W. Lee, *et al.*, Phys.Rev. **D47**, 11 (1993).

[8] L. Auerbach *et al.* (LSND), http://dx.doi.org/10.1103/PhysRevD.63.112001 Phys.Rev. **D63**, 112001 (2001), http://arxiv.org/abs/hep-ex/0101039 arXiv:hep-ex/0101039 [hep-ex] .

[9] M. Deniz *et al.* (TEXONO), http://dx.doi.org/10.1103/PhysRevD.81.072001 Phys.Rev. **D81**, 072001 (2010), arXiv:0911.1597 [hep-ex] .

[10] P. Adamson *et al.*, (2015), arXiv:1507.06690 [physics.acc-ph] .

[11] S. Agostinelli *et al.*, Nuclear Instruments and Methods in Physics Research Section A: Accelerators, Spectrometers, Detectors and Associated Equipment **506**, 250 (2003).

[12] J. Allison *et al.*, Nuclear Science, IEEE Transactions on **53**, 270 (2006).

[13] C. Alt *et al.* (NA49 Collaboration), Eur.Phys.J. **C49**, 897 (2007), http://arxiv.org/abs/hep-ex/0606028 arXiv:hep-ex/0606028 [hep-ex] .

[14] A. Ferrari, P. R. Sala, A. Fasso, and J. Ranft, (2005).

[15] G. Battistoni, S. Muraro, P. R. Sala, F. Cerutti, A. Ferrari, *et al.*, http://dx.doi.org/10.1063/1.2720455 AIP Conf.Proc. **896**, 31 (2007).

[16] A. V. Lebedev, *Ratio of pion kaon production in proton carbon interactions*, Ph.D. thesis, Harvard University (2007).

[17] L. Aliaga *et al.* (MINERvA), http://dx.doi.org/10.1016/j.nima.2013.12.053 Nucl. Instrum. Meth. **A743**, 130 (2014), http://arxiv.org/abs/1305.5199 arXiv:1305.5199 [physics.ins-det] .

[18] D. G. Michael *et al.* (MINOS Collaboration), Nucl.Instrum.Meth. **A596**, 190 (2008), http://arxiv.org/abs/0805.3170 arXiv:0805.3170 [physics.ins-det] .

[19] T. Le *et al.* (for the MINERvA), http://dx.doi.org/10.1016/j.physletb.2015.07.039 Phys. Lett. **B749**, 130 (2015), http://arxiv.org/abs/1503.02107 arXiv:1503.02107 [hep-ex] .

[20] L. Aliaga *et al.* (MINERvA), http://dx.doi.org/10.1016/j.nima.2015.04.003 Nucl. Instrum. Meth. **A789**, 28 (2015), http://arxiv.org/abs/1501.06431 arXiv:1501.06431 [physics.ins-det] .

[21] C. Andreopoulos, A. Bell, D. Bhattacharya, F. Cavanna, J. Dobson, S. Dytman, H. Gallagher, P. Guzowski, R. Hatcher, P. Kehayias, A. Meregaglia, D. Naples, G. Pearce, A. Rubbia, M. Whalley, and T. Yang, Nuclear Instruments and Methods in Physics Research Section A: Accelerators, Spectrometers, Detectors and Associated Equipment **614**, 87 (2010), Program version 2.6.2 used here.

[22] C. H. Llewellyn Smith, Phys.Rept. **3**, 261 (1972).

[23] R. Bradford, A. Bodek, H. S. Budd, and J. Arrington, http://dx.doi.org/10.1016/j.nuclphysbps.2006.08.028 Nucl.Phys.Proc.Suppl. **159**, 127 (2006), http://arxiv.org/abs/hep-ex/0602017 arXiv:hep-ex/0602017 [hep-ex] .

[24] A. Bodek, S. Avvakumov, R. Bradford, and H. S. Budd, http://dx.doi.org/10.1088/1742-6596/110/8/082004 J.Phys.Conf.Ser. **110**, 082004 (2008), http://arxiv.org/abs/0709.3538 arXiv:0709.3538 [hep-ex] .

[25] K. S. Kuzmin, V. V. Lyubushkin, and V. A. Naumov, Eur.Phys.J. **C54**, 517 (2008), http://arxiv.org/abs/0712.4384 arXiv:0712.4384 [hep-ph] .

[26] M. Day and K. S. McFarland, Phys.Rev. **D86**, 053003 (2012), http://arxiv.org/abs/1206.6745 arXiv:1206.6745 [hep-ph] .

[27] A. Bodek and J. L. Ritchie, Phys.Rev. **D23**, 1070 (1981).

[28] A. Bodek and J. L. Ritchie, Phys.Rev. **D24**, 1400 (1981).

[29] D. Rein and L. M. Sehgal, Annals Phys. **133**, 79 (1981).

[30] A. Bodek, I. Park, and U.-K. Yang, http://dx.doi.org/10.1016/j.nuclphysbps.2004.11.208 Nucl.Phys.Proc.Suppl. **139**, 113 (2005), http://arxiv.org/abs/hep-ph/0411202 arXiv:hep-ph/0411202 [hep-ph] .

[31] D. Rein and L. M. Sehgal, Nucl. Phys. **B223**, 29 (1983).

[32] J. Park, *Neutrino-Electron Scattering in MINERvA for Constraining the NuMI Neutrino Flux*, http://lss.fnal.gov/archive/thesis/2000/fermilab-thesis-2013-36.shtml Ph.D. thesis, U.

Rochester (2013).
[33] G. A. Fiorentini, D. W. Schmitz, P. A. Rodrigues, *et al.* (MINERvA Collaboration), (2013), http://arxiv.org/abs/1305.2243 arXiv:1305.2243 [hep-ex] .
[34] Z. Pavlovic, *Observation of Disappearance of Muon Neutrinos in the NuMI Beam*, Ph.D. thesis, University of Texas (2008).
[35] J. Wolcott *et al.* (MINERvA), (2015), arXiv:1509.05729 [hep-ex] .
[36] "http://www.dunescience.org," (2015).